Effects of magnetic field and twin domains on magnetostructural phase mixture in Mn_3O_4: Raman scattering studies of untwinned crystals

T. Byrum, S. L. Gleason, A. Thaler, G. J. MacDougall, and S. L. Cooper*

Department of Physics and Frederick Seitz Materials Research Laboratory, University of Illinois, Urbana, Illinois 61801, USA

(Received 1 March 2016; published 16 May 2016)

The ferrimagnetic spinel Mn_3O_4 exhibits large and anisotropic changes in electronic and structural properties in response to an applied magnetic field. These changes are thought to result from the field-dependent tuning—via strong spin-lattice coupling—between two nearly degenerate magnetostructural phases. Recent variable-magnetic-field studies of Mn_3O_4 have been performed on melt-grown crystals, which can exhibit twin domains due to a Jahn-Teller structural transition below the melting temperature. Because of the near degeneracy of the magnetostructural phases, however, strain associated with the twin domains likely affects the magnetic responses of Mn_3O_4. In this report, we present a variable-magnetic-field Raman scattering study of untwinned Mn_3O_4 crystals grown out of a flux below the Jahn-Teller structural transition. We measure distinct $\mathbf{q} = 0$ magnetic and vibrational excitation spectra for each isolated magnetostructural phase of untwinned Mn_3O_4 crystals and determine the symmetries of the observed excitations. We determine how the magnetostructural phase mixture changes in response to magnetic fields applied in the magnetic easy plane. Last, by comparing results on flux- and melt-grown Mn_3O_4 crystals, we show that the intrinsic mixture of the two magnetostructural phases is indeed strongly influenced by the presence of twin domains.

DOI: 10.1103/PhysRevB.93.184418

I. INTRODUCTION

Strongly correlated materials are characterized by a competition among multiple important interactions involving spin, charge, lattice, and orbital degrees of freedom, which often leads to a near degeneracy between competing phases [1]. Significant consequences of this near degeneracy include the coexistence of phases and/or the "colossal" tunability of physical properties in response to external perturbations such as magnetic field and pressure [2–6]. Examples of such tunable properties include multiferroic behavior [7], colossal magnetoresistance [8], magnetically tuned shape-memory effects [9,10], and magnetothermal and magnetodielectric behavior [11–13]. Clarifying the mechanisms connecting nearly degenerate phases and tunable behavior in specific materials has been one of the key challenges of condensed matter physics in recent years.

The spinel crystal structure (chemical formula AB_2X_4) is a commonly occurring structure among complex transition metal oxides and chalcogenides [14]. Many spinels display strong correlations between spin, charge, orbital, and lattice degrees of freedom due to a magnetically frustrating sublattice of corner-sharing tetrahedra [see Fig. 1(a)], as well as the anisotropy and spatial extent of the d orbitals. Consequently, a wide variety of phenomena have been reported for spinels, including superconductivity [15], charge ordering [16], heavy fermion behavior [17], and multiferroicity [18–22].

The ferrimagnetic spinel Mn_3O_4 ($A = Mn^{2+}, B = Mn^{3+}$, $X = O^{2-}$) also exhibits novel phenomena in the magnetically ordered state, including large magnetodielectric and magnetoelastic responses [13,23,24]. Magnetic-field-induced changes in the low-frequency dielectric constant and crystal dimensions have been attributed to field-induced transitions between two distinct magnetostructural phases, which are discussed below [24]. A high-resolution x-ray diffraction study recently revealed that these two magnetostructural phases in fact coexist below the Néel temperature in polycrystalline Mn_3O_4 [25], demonstrating the near degeneracy of their free energies. Thus, Mn_3O_4 belongs to the class of strongly correlated materials whose bulk physical parameters are "tunable" due to distinct phases existing in close proximity.

Mn_3O_4 is a tetragonally distorted spinel at room temperature as a result of a Jahn-Teller cubic-to-tetragonal transition at $T = 1440$ K [26]. Mn_3O_4 first magnetically orders at $T = 42$ K in a triangular configuration, with the spins lying approximately in the (100) plane and with the net magnetization along the [010] direction [27,28], where the crystallographic indices here and throughout the paper refer to the conventional (body-) centered-tetragonal setting. The c-axis components of the Mn^{3+} spins form antiferromagnetic chains along the ⟨100⟩ directions [27]. Below $T = 39$ K, an incommensurate magnetic modulation develops in half of the Mn^{3+} spins, with a propagation vector that evolves with temperature until it becomes commensurate with the lattice below $T = 34$ K, doubling the magnetic unit cell along the [010] direction [27,28].

A structural modulation with a propagation vector identical to that of the magnetic modulation has also been observed [24], demonstrating the strong spin-lattice coupling in Mn_3O_4. This strong coupling is proposed to originate from the geometric frustration of the Mn^{3+} spins, which is only partially relieved by the high-temperature, cubic-to-tetragonal distortion [24,29]. The resultant exchange striction in the magnetically ordered state leads to a cell-doubled-orthorhombic (CDO) structure whose modulation is of the form pictured in Fig. 1(b) below $T = 34$ K.

It is known that structural and magnetic symmetry changes in Mn_3O_4 can be induced with modest magnetic fields applied

*Corresponding author: slcooper@illinois.edu

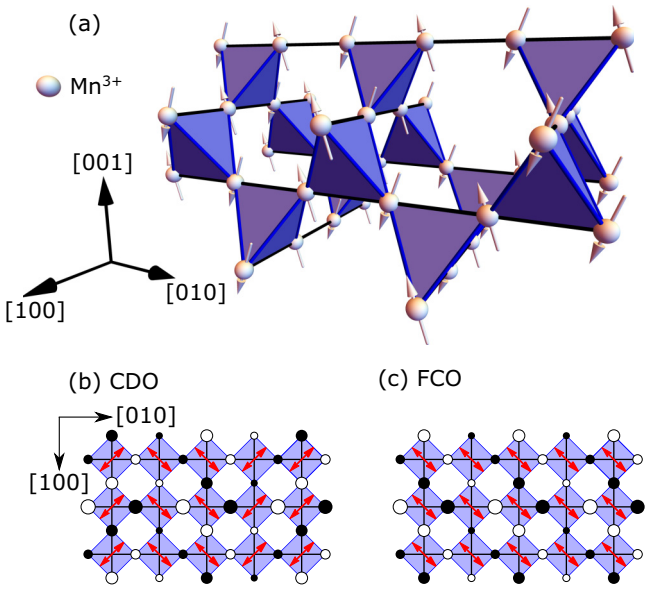

FIG. 1. (a) Schematic view of the frustrating Mn^{3+} sublattice, composed of corner-sharing tetrahedra. Antiferromagnetic chains along the [100] and [010] directions are indicated by black lines. (b, c) Proposed modulations of the Mn^{3+} spins and Mn_4^{3+} tetrahedra, given by Nii *et al.* [24] and Chung *et al.* [29], projected onto the (001) plane for the (b) cell-doubled-orthorhombic (CDO) phase and the (c) face-centered-orthombic (FCO) phase. Black and white circles specify the c-axis components of the Mn^{3+} spins and their relative sizes indicate position along the *c* axis. Red arrows indicate the local distortions of the Mn^{3+} tetrahedra.

in the (001) plane (magnetic easy plane) [10,24,30]. For example, cooling a sample in the presence of a $H = 1$ T magnetic field applied along the [110] direction drives a uniform orthorhombic distortion of the lattice via spin-orbit coupling and inverse exchange striction [24]. The resultant face-centered-orthorhombic (FCO) structure is proposed to be of the form pictured in Fig. 1(c).

Interestingly, there have been varying reports of partial or complete transitions to FCO symmetry at low temperatures even in the absence of a magnetic field, leading to phase coexistence. In single crystals of Mn_3O_4, Chung *et al.* report an instability along the [110] axis, leading to a partial FCO distortion [29], and Kim *et al.* report a complete transformation to FCO symmetry [30]. Furthermore, in a study of polycrystalline Mn_3O_4, Kemei *et al.* report a >50% FCO phase fraction at low temperatures and propose that a partial FCO transition is intrinsic and may be governed by internal strains [25]. These varying results raise questions regarding how the ground-state properties of Mn_3O_4 are affected by twin domains, impurities, and other structural properties influenced by specific crystal growth conditions.

Crystals of Mn_3O_4 are often grown out of a melt ($T_{melt} >$ 1800 K); however, such crystals may display twin domains due to the $T = 1440$ K cubic-to-tetragonal transition in this material [31,32]. The strains near twin domain walls may lead to a partial FCO transition, although this issue has yet to be explored in crystals of Mn_3O_4. Furthermore, the misalignment of twin domains prevents an external magnetic field from creating a homogeneous state. In spectroscopic studies, this inhomogeneity obscures the identification of excitations associated with specific magnetostructural phases.

In this report, we grow untwinned crystals of Mn_3O_4 from a flux at $T = 1370$ K, i.e., below the cubic-to-tetragonal transition. This allows us to study the characteristic magnons and phonons associated with each magnetostructural phase of Mn_3O_4 using Raman spectroscopy—a high-resolution ($\Delta E < 0.25$ meV) probe of the energies and symmetries of excitations in materials. We are able to isolate the CDO and FCO phases of Mn_3O_4 by applying an external magnetic field along the [010] and [110] directions, respectively, and we report the distinct $\mathbf{q} = 0$ Raman spectrum of each phase. We find that the number of modes and the polarization selection rules observed in each phase support the descriptions of the CDO and FCO phases discussed above. Finally, we obtain Raman spectra of twinned Mn_3O_4 crystals, grown from a melt for comparison, and we find that twin domains do indeed increase the FCO phase fraction present at low temperatures.

II. EXPERIMENT

A. Sample preparation

Following the work of Nielsen [31], untwinned single crystals of Mn_3O_4 were grown at the University of Illinois using a flux method. Commercial powders of manganese(II,III) oxide (Alfa-Aesar, 99.997%) and anhydrous sodium tetraborate ("Borax," Alfa-Aesar, 99.5%) were combined in a one-to-one molar ratio, wet milled under ethanol for 12 h using a FRITSCH Pulverisette P6 planetary ball mill, and dried in air at 150 °C to remove the ethanol. To control vaporization loss of Borax at high temperatures, the "crystalline seal" method developed by Wanklyn was used [33]. A double crucible was filled with the milled Mn_3O_4-Borax powder and the top was loosely sealed with a crimped-on lid. The double crucible was heated in a Lindberg/Blue box furnace to 1100 °C over 10 h, held at that temperature for 2 h, cooled to 900 °C over 12 h, and then decanted as a standard "hot-pour." The Mn_3O_4-Borax mixture that sealed the two crucibles together was dissolved by soaking the mixture alternately in deionized water and hydrochloric acid.

The untwinned Mn_3O_4 crystals were characterized with magnetization and heat capacity measurements (data shown in Appendix A), which show magnetic transitions at $T = 42$, 40, and 34 K, in good agreement with published data [27,28]. The crystallographic orientations of the samples used in this experiment were determined via x-ray diffraction measurements performed at room temperature.

The resultant crystals are long, thin parallelepipeds, with approximate dimensions $1 \times 1 \times 5$ mm. The large crystal facets are parallel to (101) and (011) planes, while the long axis is parallel to the $[\bar{1}\bar{1}1]$ direction. The facets occasionally display visible faults, and x-ray diffraction reveals that there are two twin domains present in these crystals. The twins are related by a π rotation about the long axis, and optical polarization studies confirm that the faults separate the two different crystallographic orientations. The same type of twinning has previously been observed on a microscopic scale in Mn_3O_4 grown at temperatures above the cubic-to-tetragonal

transition [34]. The twin domains of the flux-grown crystals studied in this report are macroscopic (several mm in size) and much larger than the laser spot size (∼50 μm) used in the Raman scattering experiments performed here. Consequently, we were able to obtain Raman spectra from single-domain regions of these samples; we therefore refer to these crystals as "untwinned" or "single-domain" crystals.

For comparison, microscopically twinned crystals of Mn_3O_4 were grown from a melt using a floating-zone method described by Kim *et al.* [30]. The structural and magnetic properties of the resulting crystals are reported elsewhere [10,30,35]. The crystals exhibit three magnetic transitions at $T = 43$, 39, and 33 K, consistent with previously reported temperatures [27,28]. These samples did not exhibit polarization selection rules in Raman scattering measurements, indicating that the twin domains in these samples are smaller than the laser spot size (∼50 μm) used in the Raman scattering experiments; we therefore refer to these crystals as "twinned" crystals.

B. Raman scattering measurements

Raman scattering measurements were performed using the 647.1-nm excitation line of a krypton ion laser. The incident laser power was limited to 10 mW and was focused to a ∼50-μm diameter spot to minimize laser heating of the sample, which was estimated to be roughly 4 K. The scattered light from the samples was collected in a backscattering geometry, dispersed through a triple-stage spectrometer, and detected with a liquid-nitrogen-cooled CCD detector. The incident light polarization was selected with a polarization rotator, and the scattered light polarization was analyzed with a linear polarizer, providing symmetry information about the excitations studied. The samples were inserted into a continuous He-flow cryostat, which was horizontally mounted in the open bore of a superconducting magnet, allowing Raman measurements in the temperature range $4 \leqslant T \leqslant 300$ K and the magnetic field range $0 \leqslant H \leqslant 6$ T.

Three different scattering geometries were employed in the variable-magnetic-field measurements (see Fig. 2). Each geometry shown in Fig. 2 specifies the magnetic field orientation and the plane containing the incident- and scattered-light polarizations (scattering plane). Geometry 1 (Fig. 2, left) utilizes the as-grown crystal face, which presents a (101) (or, equivalently, (011)) surface, and contains a [010] ([100]) axis. A magnetic field was applied in the scattering plane along the [010] ([100]) direction. The [010] and [100] directions become magnetically inequivalent in the magnetically ordered state, with [010] labeling the magnetization direction by convention [27]. Accordingly, when a sufficiently large magnetic field is applied along the [010] ([100]) axis to form a single magnetic domain [36], we refer to that direction as the [010] direction.

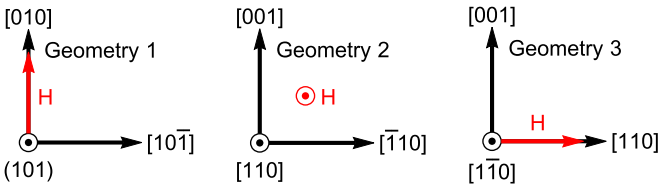

FIG. 2. Raman scattering geometries used in variable-magnetic-field measurements. Each geometry specifies the magnetic field orientation and scattering plane.

Crystals were also cut and polished to present a face normal to the [110] (or, equivalently, [1$\bar{1}$0]) direction. A magnetic field was applied either along the normal of the scattering plane (geometry 2; see Fig. 2, middle) or in the scattering plane along the [$\bar{1}$10] ([110]) direction (geometry 3; see Fig. 2, right). It is known that a sufficiently large magnetic field applied along the [110] ([$\bar{1}$10]) axis in the magnetically ordered state causes these directions to become magnetically and structurally inequivalent, as the crystal elongates along the direction of the applied magnetic field [24]. We refer to this elongated direction as the [110] direction.

III. RESULTS AND DISCUSSION

A. Room-temperature phonon spectra

Figure 3 presents the $T = 300$ K Raman spectra of an untwinned Mn_3O_4 crystal taken with various polarizations of the incident and scattered light. We observe seven of the ten Raman-active phonons predicted by a group theoretical analysis of the Mn_3O_4 crystal structure using the D_{4h} point group. The presence of polarization selection rules indicate well-defined crystallographic axes, as expected of an untwinned crystal, and the phonons exhibit symmetries consistent with the D_{4h} point group. To our knowledge, this is the first experimental determination of the Mn_3O_4 phonon symmetries.

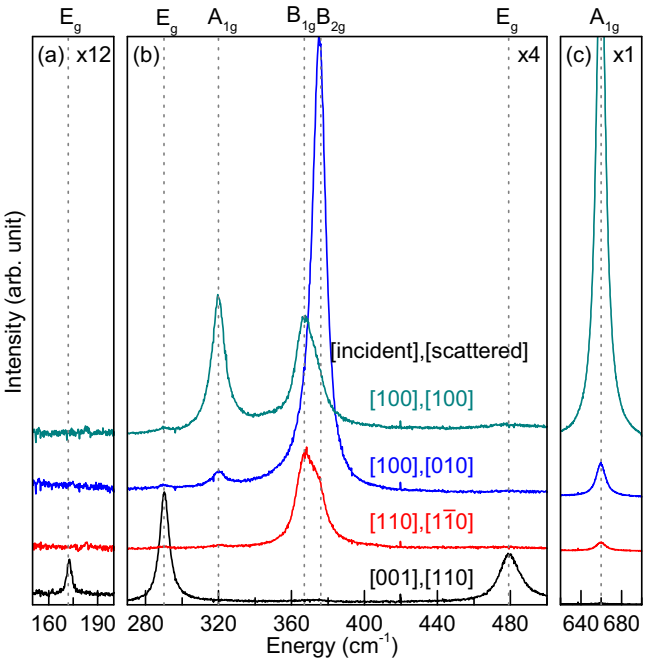

FIG. 3. Room-temperature Raman scattering spectra of Mn_3O_4 in the energy ranges (a) 150–200 cm^{-1}, (b) 270–500 cm^{-1}, and (c) 620–700 cm^{-1} at various polarizations of the incident ([hkl]) and scattered light ([h′k′l′]), as indicated by [hkl],[h′k′l′]. Phonon symmetries are specified above vertical, dashed lines that indicate the phonon peak positions. The data have been offset for clarity.

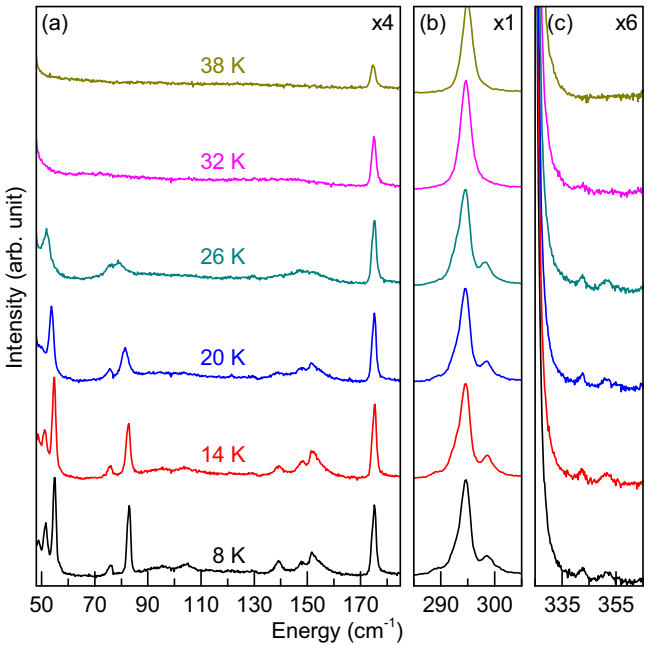

FIG. 4. Raman scattering spectra of Mn_3O_4 at various temperatures in the energy ranges (a) 50–185 cm^{-1}, (b) 285–305 cm^{-1}, and (c) 325–365 cm^{-1}. The data have been offset for clarity.

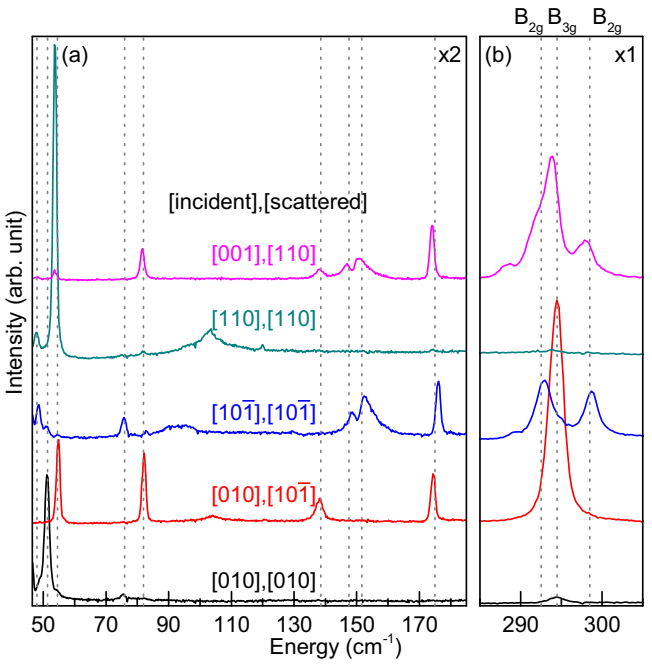

FIG. 5. Raman scattering spectra of Mn_3O_4 in the CDO phase at $T = 8$ K in the energy ranges (a) 50–185 cm^{-1} and (b) 285–305 cm^{-1} taken with various polarizations of the incident ([hkl]) and scattered light ([h′k′l′]), as indicated by [hkl], [h′k′l′]. Vertical, dashed lines indicate magnon and phonon peak positions in the CDO phase. Phonon symmetries in (b) are specified above their respective lines. The data have been offset for clarity.

In addition to demonstrating the absence of twinning in the crystals studied here, the phonon symmetry analysis in Fig. 3 shows for the first time that the large tetragonal distortion from cubic symmetry ($c/a = 1.16\sqrt{2}$) is manifest in the phonon Raman spectra. For example, we observe a 54-cm^{-1} (6.75 meV) splitting between the $\omega = 320$ cm^{-1} A_{1g} and $\omega = 374$ cm^{-1} B_{2g} phonons at room temperature; these modes are expected to be degenerate above the cubic-to-tetragonal phase transition at $T = 1440$ K [37].

B. Temperature-dependent excitation spectra

Figure 4 shows the temperature dependence of the untwinned Mn_3O_4 Raman spectrum (a) in the $50 \leqslant \omega \leqslant 185$ cm^{-1} energy range, (b) near the 295 cm^{-1} E_g phonon, and (c) in the $325 \leqslant \omega \leqslant 365$ cm^{-1} energy range. There are three salient developments in Fig. 4 for $T < 32$ K: (1) eight new peaks develop in the low-energy range $\omega < 170$ cm^{-1}, which we attribute to one-magnon excitations following the analysis of Gleason *et al.* [38]; (2) two new phonon peaks appear at $\omega = 342$ cm^{-1} and $\omega = 351$ cm^{-1}, whose energies and intensities are consistent with optical phonon modes that have been folded to the Brillouin zone center by a cell-doubling structural modulation; (3) the peak at 295 cm^{-1} develops additional structure, indicating a change in the crystal lattice structure discussed further below.

The first two features offer strong confirmation that simultaneous cell-doubling modulations of the magnetic and structural lattices develop below $T = 32$ K. Previous studies of Mn_3O_4 observed the appearance of both magnetic [24,27] and nuclear [24] superlattice reflections at $(h\ k+\frac{1}{2}\ 0)$ for integer h, k when $T < 34$ K. Figure 4 shows that, for $T < 32$ K, there is indeed a concomitant development of more than six magnon peaks and two new phonon peaks—consistent with enlarged magnetic and structural unit cells. These data provide direct spectroscopic evidence of simultaneous doubling of the magnetic and structural unit cells.

To clarify the last feature of Fig. 4 concerning a change in the crystal lattice for $T < 32$ K, we performed a polarization analysis of the magnetic and vibrational excitations. The full details of the symmetry analysis are given in Appendix B, and the experimentally determined energies and symmetries of the observed excitations are tabulated in Table I. Figure 5 shows representative spectra from this study. The symmetry selection rules exhibited by the phonon and magnon modes in Fig. 5 indicate that the low-temperature, zero-field-cooled phase of untwinned Mn_3O_4 has orthorhombic symmetry with a, b, and c axes along the [100], [010], and [001] directions, respectively.

The high-symmetry directions we observe are consistent with the modulation of the Mn_4^{3+} tetrahedra proposed by Nii *et al.* and illustrated in Fig. 1(b) [24]. We note that the displacement pattern shown in Fig. 1(b) removes the twofold rotations about the [110] and [$\bar{1}$10] axes, as well as any mirror operations in planes orthogonal to these directions. On the other hand, the twofold rotations about the [100] and [010] axes are preserved (up to a fractional translation, in the case of the [010] axis).

We clearly resolve three nondegenerate phonons near 295 cm^{-1} in the CDO phase [see Fig. 5(b)], including a B_{3g} mode ($\omega = 295$ cm^{-1}) and two B_{2g} modes ($\omega = 293$ and 298 cm^{-1}). The tetragonal-to-orthorhombic transition is expected to split the $\omega = 295$ cm^{-1} E_g phonon into a B_{3g} phonon and

a *single* B_{2g} phonon. The presence of a second B_{2g} phonon is associated with a phonon mode that has been folded to $\mathbf{q} = 0$ because of the cell-doubling structural modulation that occurs for $T < 32$ K, similar to the folded phonon modes at $\omega = 342$ and 351 cm^{-1} discussed previously.

Based on the number of modes we observe and their respective polarization selection rules, we conclude that untwinned Mn_3O_4 transitions to the CDO phase depicted in Fig. 1(b) for $T < 32$ K in the absence of a magnetic field. An explanation for reports of partial or complete transitions to an FCO phase at low temperatures is given in Sec. III D.

C. Magnetic-field-dependent excitation spectra

Previous studies [10,24,30] have shown that an applied magnetic field can significantly influence the crystal lattice of Mn_3O_4, and that the field-induced structural changes depend on the orientation of the applied field. For example, a recent x-ray and neutron scattering study by Nii *et al.* reported that a magnetic field applied along the [110] direction stabilizes the FCO phase with a, b, and c axes along the $[1\bar{1}0]$, [110], and [001] directions, respectively [24]. Additionally, no satellite peaks were observed in neutron and x-ray diffraction measurements of the FCO phase, indicating the structural and magnetic modulations are absent in this phase [24]. Our spectroscopic studies of untwinned Mn_3O_4 allow a further elucidation of the magnetic-field-induced phases of Mn_3O_4, by allowing us to study *simultaneously* the magnetic and phonon excitation spectra while applying a magnetic field along well-defined crystallographic directions. We will first show that a magnetic field applied along the [110] direction does indeed lead to a transition to the FCO magnetostructural phase. Next, we will show that a magnetic field applied along the [010] direction preserves the CDO magnetostructural phase. However, we will also show that reversing the magnetic field from [010] to $[0\bar{1}0]$ induces a CDO $\rightarrow$ FCO $\rightarrow$ CDO transition.

1. H ∥ [110]: *Face-centered-orthorhombic phase*

Figure 6 shows the magnetic-field dependence of the Raman spectrum in the energy ranges $50 \leqslant \omega \leqslant 185$ cm^{-1} and $285 \leqslant \omega \leqslant 305$ cm^{-1} for a magnetic field applied along the [110] direction measured in Figs. 6(a) and 6(b) in geometry 2 and in Figs. 6(c) and 6(d) in geometry 3 at $T = 8$ K. The two scattering geometries are employed to allow the observation of nearly all of the Raman-active modes. For all measurements, the sample was zero-field-cooled from room temperature to $T = 8$ K before a magnetic field was applied. The resulting $H = 0$ T and $T = 8$ K Raman spectra [bottom curves in Figs. 6(a) and 6(b)] are consistent with the CDO phase, as discussed in Sec. III B [40]. When $\mathbf{H} \parallel [110]$, as the magnetic field magnitude is increased, the spectra in Fig. 6 change dramatically in the range $0 \leqslant H \leqslant 1$ T, indicating a magnetostructural phase transition. No further changes in the spectra are observed for $1 < H \leqslant 6$ T (data not shown). We show below that the phase stabilized for $H > 1$ T with $\mathbf{H} \parallel [110]$ is consistent with the FCO phase, in agreement with the results of Nii *et al.* [24].

To verify the FCO symmetry of the magnetostructural phase for $H > 1$ T and $\mathbf{H} \parallel [110]$, we performed a polarization

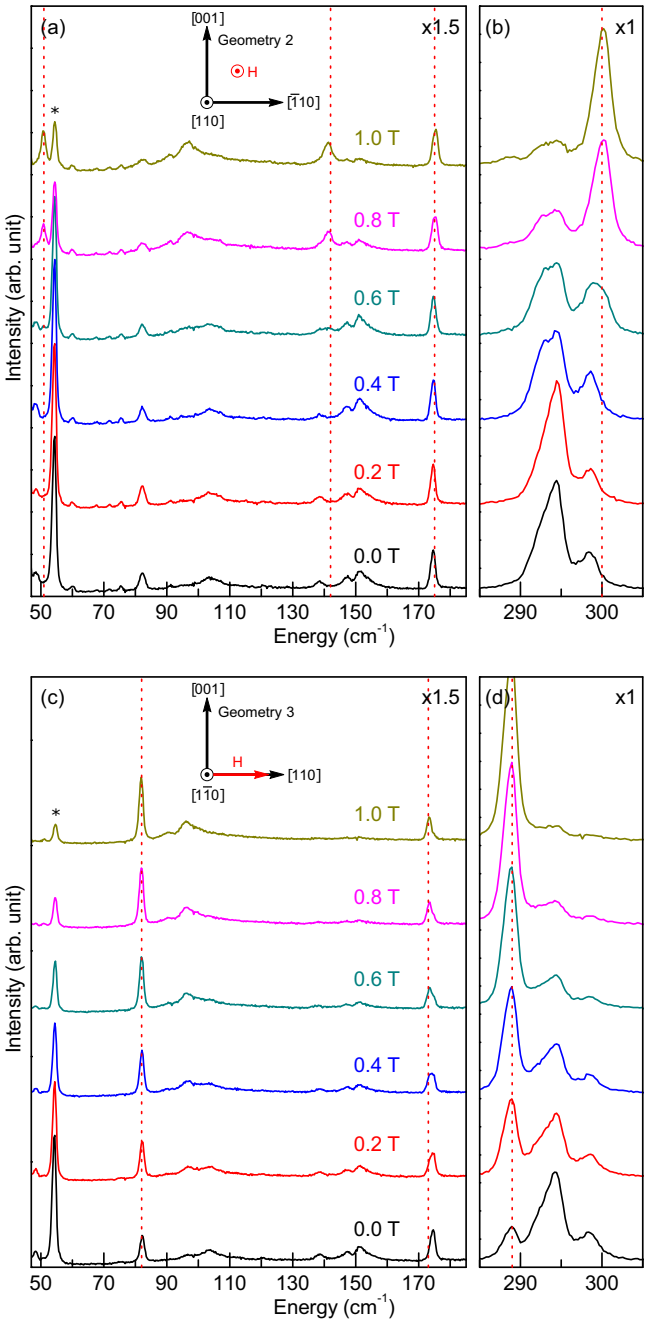

FIG. 6. Raman scattering spectra of Mn_3O_4 at $T = 8$ K taken in (a, b) geometry 2 and (c, d) geometry 3 (see Sec. II B) at various magnetic fields in the energy ranges (a, c) 50–185 cm^{-1} and (b, d) 285–305 cm^{-1}. Vertical, dashed lines indicate magnon and phonon peak positions in the FCO phase. The asterisk indicates a peak associated with a small, remnant CDO phase fraction [39]. The data have been offset for clarity.

study of the magnetic and vibrational excitations in this phase regime. The full details of the symmetry analysis are given in Appendix B, and the experimentally determined energies and symmetries of the observed excitations are tabulated in Table I. Figure 7 shows representative spectra from this study. The broad, asymmetric peak at $\omega = 96$ cm^{-1} in the FCO phase is identified as a two-magnon excitation based on the analysis

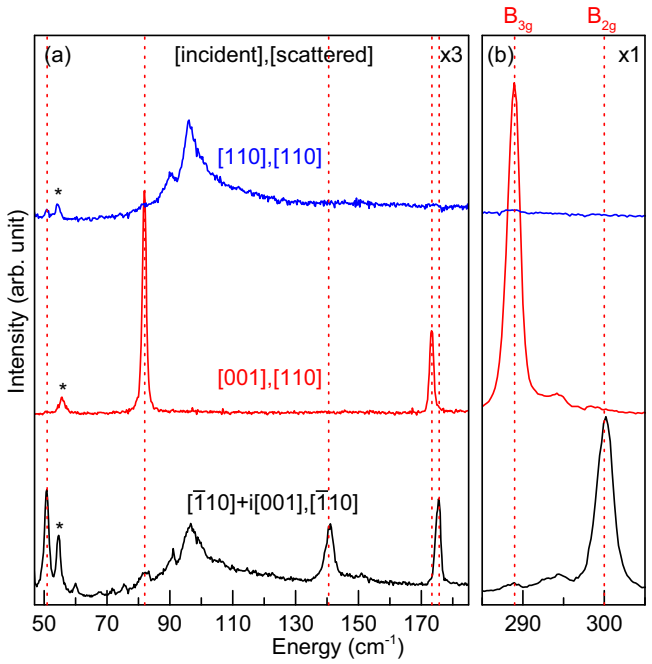

FIG. 7. Raman scattering spectra of Mn_3O_4 in the FCO phase at $T = 8$ K and $H = 1$ T along the [110] direction in the energy ranges (a) 50–185 cm^{-1} and (b) 285–305 cm^{-1} taken with various polarizations of the incident ([hkl]) and scattered light ([h′k′l′]), as indicated by [hkl],[h′k′l′]. ($[h_1k_1l_1] + i[h_2k_2l_2]$ denotes circular polarization.) Vertical, dashed lines indicate magnon and phonon peak positions in the FCO phase. Phonon symmetries in (b) are specified above their respective lines. The asterisk indicates a peak associated with a small, remnant CDO phase fraction [39]. The data have been offset for clarity.

of Gleason *et al.* and will not be discussed [38]. The phonon and magnon modes exhibit symmetry selection rules that are consistent with an FCO structure having a, b, and c axes along the [1$\bar{1}$0], [110], and [001] directions, respectively. These new high-symmetry axes can be understood by examining the displacement pattern proposed by Nii *et al.* [24] and depicted in Fig. 1(c). The uniform distortion of the Mn_4^{3+} tetrahedra removes the twofold rotational symmetry about the [100] and [010] axes, as well as the mirror operations in planes orthogonal to these directions. On the other hand, the lattice depicted in Fig. 1(c) possesses twofold rotational symmetry about the [110] and [$\bar{1}$10] directions, which is consistent with the selection rules we observe. Furthermore, the splitting between the two normal modes near 295 cm^{-1} is ∼11 cm^{-1} in the FCO phase, which is ∼4 times larger than the splitting between the equivalent modes in the CDO phase. As this splitting reflects the loss of fourfold symmetry in the (001) plane, a larger splitting in the FCO phase makes sense, given the more pronounced asymmetry between the in-plane, high-symmetry directions caused by the uniform distortion of the crystal.

To complete the characterization of the FCO phase, we examined the folded optical phonons, which are a signature of the structural cell-doubling modulation. Figure 8 shows the magnetic-field dependence of (a) the phonon spectrum in the $285 \leqslant \omega \leqslant 305$ cm^{-1} energy range and (b) the folded

TABLE I. Measured energies and symmetries of the magnetic and vibrational excitations in the CDO and FCO phases of Mn_3O_4 at $T = 8$ K. See Appendix B for details. The energy difference between the B_{2g} and B_{3g} phonons at $\omega = 175$ cm^{-1} could not be resolved in the CDO phase.

	Energy (cm^{-1})		
	CDO phase	FCO phase	$\Gamma(D_{2h})$
Magnon	49	–	A_g
	51	51	A_g
	54	–	B_{1g}
	–	56	B_{1g}
	75	–	A_g
	83	83	B_{3g}
	139	–	B_{3g}
	–	142	B_{2g}
	148	–	B_{2g}
	152	–	B_{2g}
Phonon	–	174	B_{3g}
	175	–	B_{2g}
	175	–	B_{3g}
	–	176	B_{2g}
	–	289	B_{3g}
	293	–	B_{2g}
	295	–	B_{3g}
	298	–	B_{2g}
	–	300	B_{2g}

phonons near 342 cm^{-1} and 351 cm^{-1} for $\mathbf{H} \parallel [110]$ and $T = 8$ K. As discussed above, the $H = 0$ T phonon and magnon spectra of untwinned Mn_3O_4 below $T = 32$ K are indicative of the CDO phase [40]. When $\mathbf{H} \parallel [110]$, the intensities of the folded phonons diminish with increasing magnetic field. For $H > 2$ T, the folded phonon modes vanish as the FCO phase is stabilized, as indicated by the appearance of the $\omega = 300$ cm^{-1} phonon and the suppression of the $\omega = 293$, 295, and 298 cm^{-1} phonons in Fig. 8(a) [compare with field dependence in Fig. 6(b)]. This field dependence confirms that a magnetic field applied along the [110] direction suppresses the cell-doubling *structural* modulation in Mn_3O_4, consistent with the results of Nii *et al.* [24] Additionally, we observe fewer than six magnons in the FCO phase, as seen in Fig. 6, consistent

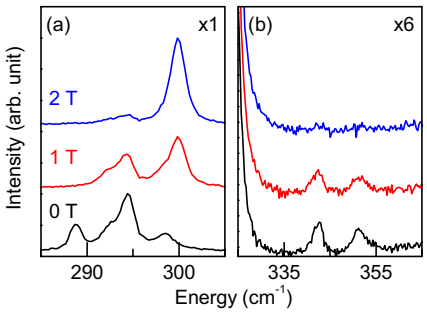

FIG. 8. Raman scattering spectra of Mn_3O_4 at $T = 8$ K taken in geometry 2 (see Sec. II B) at various magnetic fields in the energy ranges (a) 285–305 cm^{-1} and (b) 325–365 cm^{-1}. The data have been offset for clarity.

with the number of spins in the FCO unit cell, indicating the *magnetic* cell-doubling modulation is not present in the FCO phase. These data provide further evidence that the structural and magnetic cell-doubling modulations are absent in the FCO phase.

A summary of the CDO and FCO excitation spectra is given in Table I, which tabulates the experimentally determined energies and symmetries of the Raman-active one-magnon and one-phonon excitations with $\omega \leqslant 300$ cm^{-1} for the CDO and FCO phases. Each normal mode can be assigned to an irreducible representation of the D_{2h} point group. The details of the analysis performed are given in Appendix B.

2. H ∥ [010]: *Cell-doubled-orthorhombic phase*

We next show that a magnetic field applied along the magnetic easy axis [010] preserves the CDO phase in untwinned Mn_3O_4. Figure 9 shows the magnetic-field dependence of the Raman spectrum (a) in the $50 \leqslant \omega \leqslant 185$ cm^{-1} energy range and (b) near 295 cm^{-1} for **H** ∥ [010] at $T = 8$ K. The sample was zero-field-cooled from room temperature to $T = 8$ K before the magnetic field was applied. Once again, the $H = 0$ T Raman spectrum of untwinned Mn_3O_4 (bottom curve) is characteristic of the CDO phase [40].

As the magnetic field is increased to $H = 1$ T, the spectrum does not change appreciably. Moreover, no significant changes are observed in the spectrum for magnetic fields up to $H = 6$ T (data not shown). We conclude that the CDO phase is stable for a magnetic field applied along the [010] direction in Mn_3O_4.

Previous Raman scattering studies by Kim *et al.* reported that an FCO phase can be stabilized for magnetic fields applied in the (001) plane [10,30]. Indeed, our phonon Raman data are qualitatively similar to those of Kim *et al.* [41]. However, Kim *et al.* reported that the FCO phase is stabilized for an $H > 3$ T magnetic field oriented either along or orthogonal to the easy axis direction ([010]) [10,30], which conflicts with the results in Sec. III C 1 and Sec. III C 2 of this paper. Our results, as well as the results of Nii *et al.* [24], suggest that magnetic fields that stabilized the FCO phase in Refs. [10] and [30] were actually along the [$\bar{1}$10] or [110] directions. This discrepancy likely results from an inconsistent use of both face-centered-tetragonal and body-centered-tetragonal settings when describing crystallographic orientations in Refs. [10] and [30].

3. H ∥ [010]: *Phase hysteresis*

After applying a magnetic field along the [010] direction and subsequently reducing the field to $H = 0$ T, we occasionally found that the CDO spectrum would transform to the FCO spectrum. This motivated us to perform a sequence of measurements in which a magnetic field applied along the [010] direction was cycled between $H = +0.3$ and $H = -0.3$ T. Figure 10 shows the Raman spectra of Mn_3O_4 for various fields in this sequence.

Figure 10 demonstrates that reversing a magnetic field along the [010] direction can dramatically influence the phase fraction of Mn_3O_4. We have already identified and attributed the $H = \pm 0.3$ T Raman spectra (marked in black) to the CDO phase. The red spectrum observed at $H = \pm 0.05$ T is the FCO spectrum formerly obtained by applying a $H = 1$ T magnetic

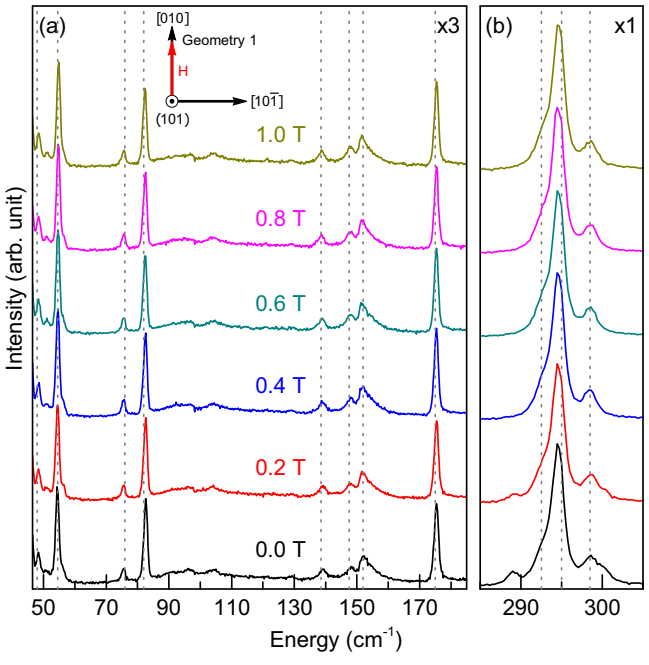

FIG. 9. Raman scattering spectra of Mn_3O_4 at $T = 8$ K taken in geometry 1 (see Sec. II B) at various magnetic fields in the energy ranges (a) 50–185 cm^{-1} and (b) 285–305 cm^{-1}. Vertical, dashed lines indicate magnon and phonon peak positions in the CDO phase. The data have been offset for clarity.

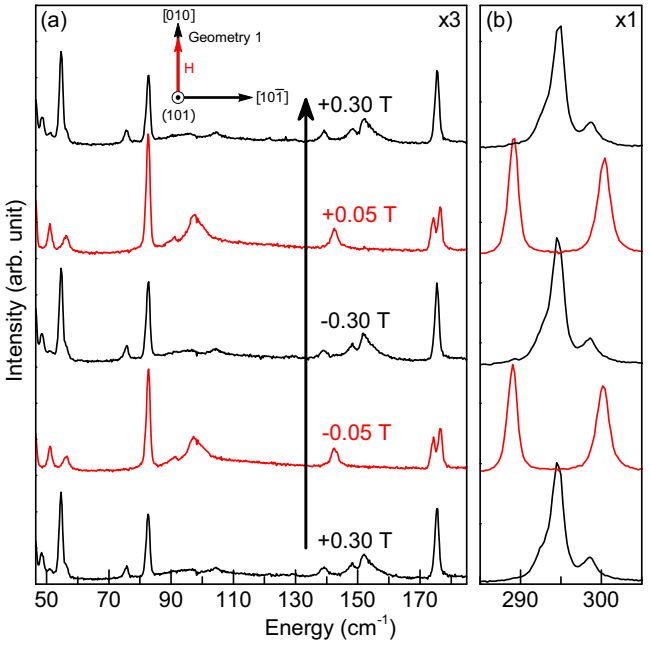

FIG. 10. Raman scattering spectra of Mn_3O_4 at $T = 8$ K taken in geometry 1 (see discussion in Sec. II B) at various magnetic fields in the energy ranges (a) 50–185 cm^{-1} and (b) 285–305 cm^{-1}. The Raman spectrum for the CDO and FCO phases are marked in black and red, respectively. The arrow indicates the sequence of field values used. The data have been offset for clarity.

field along the [110] direction, which can be seen by comparing the peaks in this spectrum with those in the $H = 1$ T spectra in Fig. 6.

Note that we previously demonstrated that a magnetic field along the [010] direction stabilizes the CDO phase. Remarkably, if the magnetic field is applied along the [010] direction and subsequently reversed to the [0$\bar{1}$0] direction, the phase fractions change dramatically near $H = 0$ T. In fact, the crystal intermediately transitions fully to the FCO phase before reverting to the CDO phase at higher field strengths. The ability to tune between the CDO and FCO phases with very small magnetic fields along the [010] direction further illustrates that the free energies of these two phases are nearly degenerate in Mn_3O_4 at $T = 8$ K.

D. Effect of twin domains

We have identified the distinct Raman spectra of the CDO and FCO phases of Mn_3O_4 at low temperatures. The near degeneracy of these phases is evidenced by the ability to manipulate the phase fraction at low temperature with modest magnetic fields applied in the (001) plane. Consequently, it is likely that other parameters, e.g., strain, can also influence the phase fraction of Mn_3O_4. Indeed, an x-ray diffraction study by Kemei *et al.* reported phase coexistence in polycrystalline Mn_3O_4 at low temperatures, which was attributed to strain arising from domain walls [25].

It is well established that growth temperature contributes to the presence or absence of structural domains in crystals of Mn_3O_4. As discussed in Sec. I, twin domains can be introduced in Mn_3O_4 crystals by growing at temperatures above the $T = 1440$ K cubic-to-tetragonal Jahn-Teller transition, e.g., by growing crystals from a melt [31,32]. On the other hand, untwinned Mn_3O_4 crystals can be obtained by growing at temperatures below the Jahn-Teller transition, e.g., from a flux [31] or via chemical vapor transport [32].

To study the effect of structural domains on the low-temperature phase fraction in Mn_3O_4 crystals, we compared Raman scattering spectra from both untwinned and twinned Mn_3O_4 crystals in the absence of a magnetic field. Figure 11 shows the zero-field-cooled, $T = 8$ K Raman spectra of multiple untwinned and twinned Mn_3O_4 crystals. The untwinned crystals overwhelmingly exhibit the CDO phase, while the twinned crystals exhibit a coexistence of both CDO and FCO phases. This indicates that the low-temperature FCO phase fraction is strongly influenced by the presence of structural domains in Mn_3O_4 crystals, with structural domains promoting the nucleation of the FCO phase.

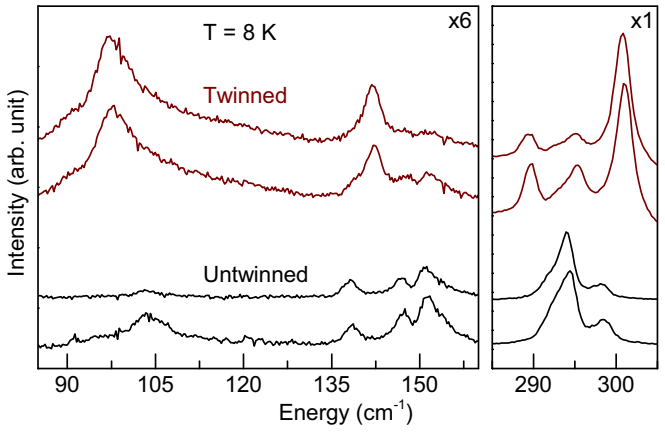

FIG. 11. Raman scattering spectra of untwinned and twinned Mn_3O_4 crystals at $T = 8$ K in the energy ranges (a) 85–160 cm^{-1} and (b) 285–305 cm^{-1}. The data have been offset for clarity.

As the anisotropic responses of the electronic and structural properties of Mn_3O_4 to an applied magnetic field are thought to result from tuning between the CDO and FCO phases, controlling the phase fraction via the introduction of structural domains may present a novel mechanism for controlling the functional behavior of Mn_3O_4.

IV. SUMMARY

We performed a variable-temperature and variable-magnetic-field Raman scattering study of untwinned Mn_3O_4 crystals. By studying untwinned crystals, we are able to identify the distinctive $\mathbf{q} = 0$ magnetic and vibrational Raman excitation energies and symmetries of Mn_3O_4 for both the CDO and FCO phases at $T = 8$ K. Our spectroscopic results for each phase support the microscopic description of the two magnetostructural phases given by Nii *et al.* [24] We also report the effects of a magnetic field applied in the (001) plane on the magnetostructural phase mixture of Mn_3O_4 at $T = 8$ K. Specifically, we find that field orientations $\mathbf{H} \parallel [010]$ and $\mathbf{H} \parallel [110]$ for $H > 1$ T select the CDO and FCO phases, respectively, in untwinned Mn_3O_4. Last, we compare the $H = 0$ T, $T = 8$ K Raman spectra of untwinned crystals to the spectra of twinned crystals of Mn_3O_4. We find that the presence of twin domains increases the low-temperature phase fraction of the FCO phase in crystals of Mn_3O_4. This result may explain the varying reports of partial or complete transitions to the FCO phase and also suggests a mechanism for controlling the low-temperature phase and functional behavior of Mn_3O_4.

ACKNOWLEDGMENTS

Research by T.B., S.L.G., and S.L.C. was supported by the National Science Foundation under Grant No. NSF DMR 14-64090. Research by A.T. and G.J.M. was supported by the NSF under Grant No. DMR-1455264-CAR.

T. Byrum and S. L. Gleason contributed equally to this work.

APPENDIX A: SAMPLE CHARACTERIZATION

We collected DC magnetization data using a Quantum Design MPMS-3 (see Fig. 12), as well as heat capacity data using a Quantum Design PPMS-DynaCool (see Fig. 13). Both zero-field-cooled and field-cooled data are shown. The data show magnetic transitions at $T = 42$, 40, and 34 K, in good agreement with published data [27,28]. The apparent 0.5 K splitting of the $T = 34$ K cell-doubling transition in Fig. 13 is an artifact of the method by which we collected our data—one peak is from the warming part of the cycle, while the other is from the cooling section. As discussed by Guillou *et al.*, this is a clear signature of a first-order phase transition [42]. It also suggests that the quality of these crystals is high, as

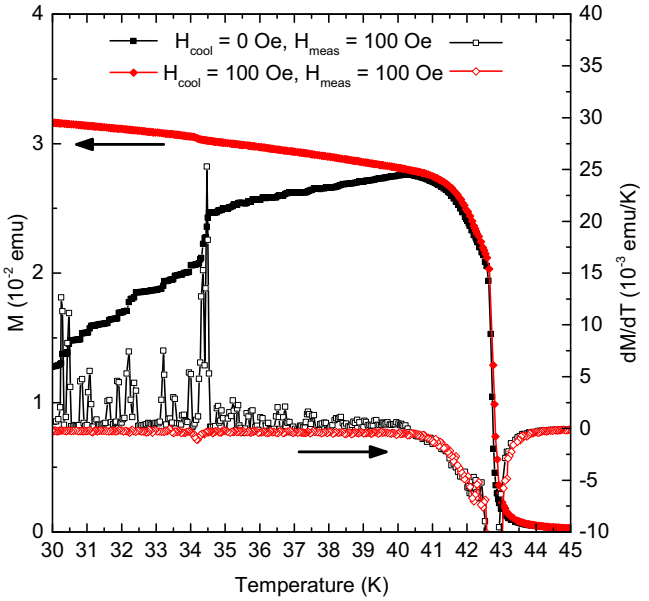

FIG. 12. DC magnetization measurements, including both zero-field-cooled (black) and field-cooled (red) data. Closed and open symbols correspond to magnetization and its temperature derivative, respectively.

low-quality, multigrain crystals have transition temperatures that are too smeared out to see such sharp features.

APPENDIX B: POLARIZATION STUDIES

At room temperature, the Bravais lattice of Mn_3O_4 is centered tetragonal. Two equivalent conventional unit cells are employed in the literature: a body-centered-tetragonal cell

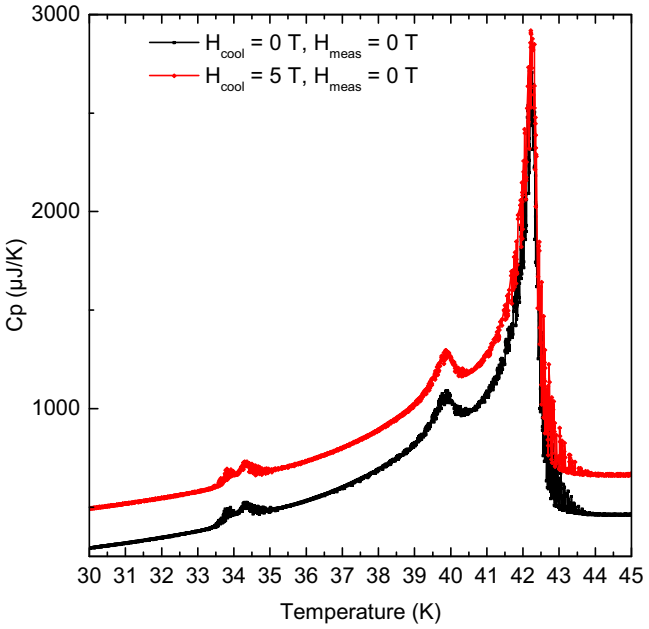

FIG. 13. Heat capacity measurements, including both zero-field-cooled (black) and field-cooled (red) data.

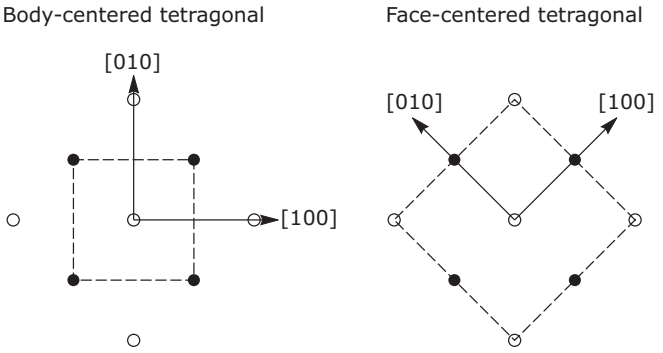

FIG. 14. Illustration showing the equivalence of body-centered-tetragonal and face-centered-tetragonal Bravais lattices. White and black circles denote lattice points at different c-axis positions.

(Fig. 14, left) and a face-centered-tetragonal cell (Fig. 14, right). These coordinate systems differ by a $\pi/4$ rotation about the [001] axis. In this paper, we choose the body-centered-tetragonal setting as our coordinate system.

At room temperature, the Mn_3O_4 crystal structure possesses fourfold rotational symmetry about the principal axis [001], up to a fractional translation. The crystal structure also has two pairs of twofold symmetry axes in the (001) plane: the secondary axes [100] and [010] and the tertiary axes [$\bar{1}$10] and [110].

The low-temperature, orthorhombic magnetostructural phases of Mn_3O_4, which form the subject of this paper, are distorted such that fourfold symmetry is lost. Each phase retains only *one* pair of twofold symmetry axes in the (001) plane. The cell-doubled-orthorhombic (CDO) phase retains twofold symmetry about the [100] and [010] directions (see Fig. 15, left). Because the cell-doubling modulation present in this phase leads to a unit cell that is not internally centered, we refer to this phase as cell-doubled orthorhombic rather than body-centered orthorhombic. On the other hand, the face-centered-orthorhombic (FCO) phase retains twofold symmetry about the [$\bar{1}$10] and [110] directions (see Fig. 15, right).

Table II presents the D_{2h} Raman tensors for each phase with respect to the body-centered-tetragonal coordinate system.

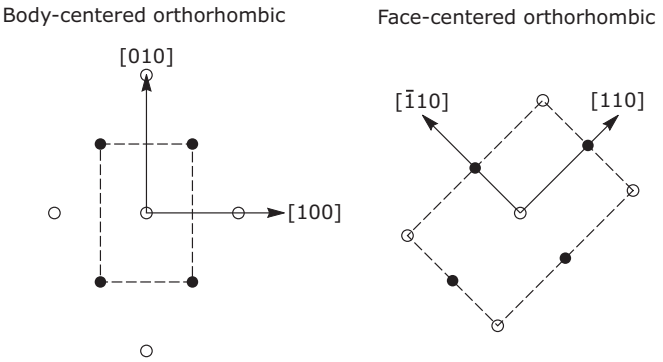

FIG. 15. Illustration of body-centered-orthorhombic and FCO Bravais lattices. White and black circles denote lattice points at different c-axis positions. Crystallographic directions are with respect to the body-centered-tetragonal coordinate system.

TABLE II. D_{2h} Raman tensors for the CDO and FCO phases in the body-centered-tetragonal coordinate system.

CDO Raman tensors				FCO Raman tensors			
A_g	B_{1g}	B_{2g}	B_{3g}	A_g	B_{1g}	B_{2g}	B_{3g}
$\begin{pmatrix} a & 0 & 0 \\ 0 & b & 0 \\ 0 & 0 & c \end{pmatrix}$	$\begin{pmatrix} 0 & d & 0 \\ d & 0 & 0 \\ 0 & 0 & 0 \end{pmatrix}$	$\begin{pmatrix} 0 & 0 & e \\ 0 & 0 & 0 \\ e & 0 & 0 \end{pmatrix}$	$\begin{pmatrix} 0 & 0 & 0 \\ 0 & 0 & f \\ 0 & f & 0 \end{pmatrix}$	$\begin{pmatrix} \frac{a+b}{2} & \frac{b-a}{2} & 0 \\ \frac{b-a}{2} & \frac{a+b}{2} & 0 \\ 0 & 0 & c \end{pmatrix}$	$\begin{pmatrix} d & 0 & 0 \\ 0 & -d & 0 \\ 0 & 0 & 0 \end{pmatrix}$	$\begin{pmatrix} 0 & 0 & \frac{e}{\sqrt{2}} \\ 0 & 0 & \frac{e}{\sqrt{2}} \\ \frac{e}{\sqrt{2}} & \frac{-e}{\sqrt{2}} & 0 \end{pmatrix}$	$\begin{pmatrix} 0 & 0 & \frac{f}{\sqrt{2}} \\ 0 & 0 & \frac{f}{\sqrt{2}} \\ \frac{f}{\sqrt{2}} & \frac{f}{\sqrt{2}} & 0 \end{pmatrix}$

TABLE III. Incident and scattered polarizations with expected amplitudes for each scattering geometry. ($[h_1k_1l_1] + i[h_2k_2l_2]$ denotes circular polarization.)

Polarization		CDO amplitude $\lvert\hat{\mathbf{E}}_s \chi \hat{\mathbf{E}}_i\rvert^2$			
Incident ($\mathbf{E_i}$)	Scattered ($\mathbf{E_s}$)	A_g	B_{1g}	B_{2g}	B_{3g}
$[10\bar{1}]$	$[10\bar{1}]$	$0.1a^2 + 0.4ac + 0.5c^2$		$0.8e^2$	
[001]	$[\bar{1}10]$			$0.5e^2$	$0.5f^2$
$[\bar{1}10]$	$[\bar{1}10]$	$0.5(a+b)^2$	d^2		
$[10\bar{1}] + i[010]$	[010]	$0.5b^2$	$0.1d^2$		$0.4f^2$
$[10\bar{1}]$	[010]		$0.3d^2$		$0.7f^2$
[010]	[010]	b^2			
$[10\bar{1}] + i[010]$	$[10\bar{1}]$	$0.2ac + 0.3c^2$	$0.1d^2$	$0.4e^2$	$0.4f^2$

Symmetric tensors were found sufficient to describe the polarization dependencies observed for each peak's intensity. Magnetic excitations are assigned to irreducible representations of the D_{2h} point group, rather than the monoclinic magnetic point group reported by Jensen *et al.* [27], for the same reason.

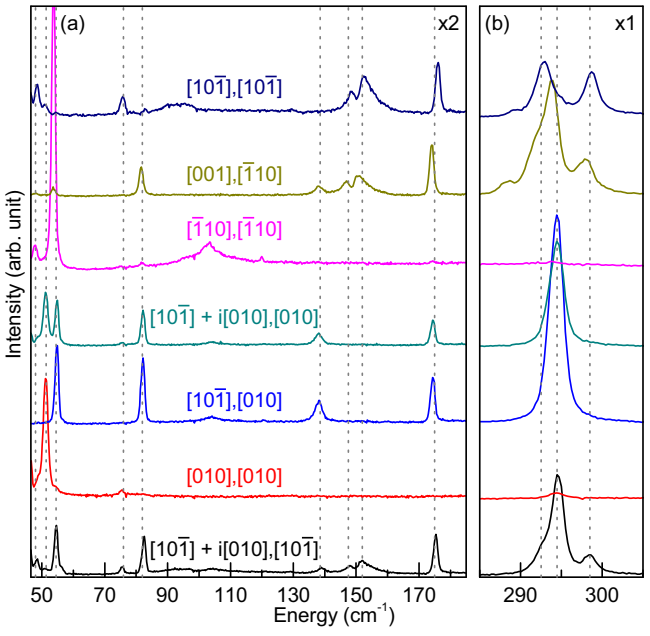

FIG. 16. Raman scattering spectra of Mn_3O_4 in the CDO phase at $T = 8$ K in the energy ranges (a) 50–185 cm^{-1} and (b) 285–305 cm^{-1} taken with various polarizations of the incident ([hkl]) and scattered light ([h′k′l′]), as indicated by [hkl], [h′k′l′]. ($[h_1k_1l_1] + i[h_2k_2l_2]$ denotes circular polarization.) Vertical, dashed lines indicate magnon and phonon peak positions in the CDO phase. The data have been offset for clarity.

1. Cell-doubled-orthorhombic phase

Seven configurations of incident and scattered light polarizations were used to determine the symmetries of excitations present in the CDO phase of Mn_3O_4. Each sample was field-trained to create a single domain prior to measurement. The obtained spectra are shown in Fig. 16. For each polarization configuration, the scattering amplitudes of the irreducible representations of the D_{2h} point group are tabulated in Table III.

Each CDO normal mode can be assigned to an irreducible representation of the D_{2h} point group using the CDO Raman tensors presented in Table II. This is *not* possible using the FCO Raman tensors, indicating that the high-symmetry directions

TABLE IV. Energies and symmetries of the magnetic and vibrational excitations in the CDO phase at $T = 8$ K. The energy difference between the B_{2g} and B_{3g} phonons at $\omega = 175$ cm^{-1} could not be resolved in this phase.

CDO excitation symmetries		
Excitation	Energy (cm^{-1})	Γ (D_{2h})
Magnon	49	A_g
	51	A_g
	54	B_{1g}
	75	A_g
	83	B_{3g}
	139	B_{3g}
	148	B_{2g}
	152	B_{2g}
Phonon	175	B_{2g}
	175	B_{3g}
	293	B_{2g}
	295	B_{3g}
	298	B_{2g}

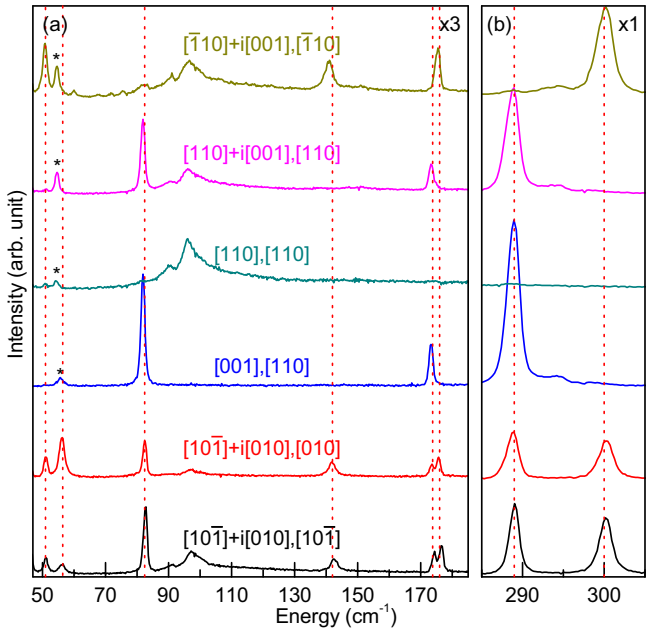

FIG. 17. Raman scattering spectra of Mn_3O_4 in the FCO phase at $T = 8$ K in the energy ranges (a) 50–185 cm^{-1} and (b) 285–305 cm^{-1} taken with various polarizations of the incident ([hkl]) and scattered light ([h′k′l′]), as indicated by [hkl], [h′k′l′]. ($[h_1k_1l_1] + i[h_2k_2l_2]$ denotes circular polarization.) Vertical, dashed lines indicate magnon and phonon peak positions in the FCO phase. The asterisk indicates a peak associated with a remnant CDO phase. The data have been offset for clarity.

in the CDO phase are along the [100] and [010] directions, as described previously. The experimentally determined energies and symmetries of the Raman-active magnetic and vibrational excitations with $\omega \leqslant 300$ cm^{-1} are tabulated in Table IV. We note that the Raman tensor of the $\omega = 51$ cm^{-1} A_g mode appears to have $a \simeq -b$, suggesting that this normal mode originates from a B_{1g} mode in the tetragonal (D_{4h}) phase.

2. Face-centered-orthorhombic phase

Six configurations of incident and scattered light polarizations were used to determine the symmetries of excitations present in the FCO phase of Mn_3O_4. Again, each sample was field-trained to create a single domain prior to measurement. The obtained spectra are shown in Fig. 17. For each polarization configuration, the scattering amplitudes of the irreducible representations of the D_{2h} point group are tabulated in Table V.

Each FCO normal mode can be assigned to an irreducible representation of the D_{2h} point group using the FCO Raman tensors presented in Table II. This is *not* possible using the CDO Raman tensors, indicating that the high-symmetry directions in the FCO phase are along the [$\bar{1}$10] and [110] directions, as described previously. The experimentally determined energies and symmetries of the Raman-active magnetic and vibrational excitations with $\omega \leqslant 300$ cm^{-1} are tabulated in Table VI. The broad, asymmetric peak at $\omega = 96$ cm^{-1} in the FCO phase is identified as a two-magnon excitation based on the analysis of Gleason *et al.* [38] and will not be discussed.

Determining the symmetry of the $\omega = 56$ cm^{-1} magnetic excitation is complicated by the peak at $\omega = 54$ cm^{-1}, which is a peak exclusive to the Raman spectrum of the CDO phase. To see this, note that the $\omega = 54$ cm^{-1} peak has a large scattering cross-section, as seen in Fig. 16. The nonzero peak intensity at $\omega = 54$ cm^{-1} in the FCO phase (Fig. 17) is due to the presence of a small, remnant CDO phase fraction indicated by a nonzero peak intensity at $\omega = 295$ cm^{-1}. In our analysis, we conclude that the peak at $\omega = 56$ cm^{-1} is absent in all but the bottom two curves in Fig. 17.

TABLE VI. Energies and symmetries of the magnetic and vibrational excitations in the FCO phase at $T = 8$ K.

FCO excitation symmetries		
Excitation	Energy (cm^{-1})	Γ (D_{2h})
Magnon	51	A_g
	56	B_{1g}
	83	B_{3g}
	142	B_{2g}
Phonon	174	B_{3g}
	176	B_{2g}
	289	B_{3g}
	300	B_{2g}

TABLE V. Incident and scattered polarizations as well as the expected amplitudes for each scattering geometry. ($[h_1k_1l_1] + i[h_2k_2l_2]$ denotes circular polarization.)

Polarization		FCO amplitude $\lvert\hat{\mathbf{E}}_s\chi\hat{\mathbf{E}}_i\rvert^2$			
Incident ($\mathbf{E_i}$)	Scattered ($\mathbf{E_s}$)	A_g	B_{1g}	B_{2g}	B_{3g}
[$\bar{1}$10] + i[001]	[$\bar{1}$10]	$0.5a^2$		$0.5e^2$	
[110] + i[001]	[001]	$0.5b^2$			$0.5f^2$
[110]	[110]	b^2			
[001]	[110]				f^2
[10$\bar{1}$] + i[010]	[010]	$0.2a^2 + 0.2ab + 0.2b^2$	$0.5d^2$	$0.2e^2$	$0.2f^2$
[10$\bar{1}$] + i[010]	[10$\bar{1}$]	$0.1ac + 0.1bc + 0.3c^2$		$0.4e^2$	$0.4f^2$

[1] E. Dagotto, Science **309**, 257 (2005).

[2] E. Dagotto, S. Yunoki, C. Şen, G. Alvarez, and A. Moreo, J. Phys.: Condens. Matter **20**, 434224 (2008).

[3] K. H. Ahn, T. F. Seman, T. Lookman, and A. R. Bishop, Phys. Rev. B **88**, 144415 (2013).

[4] J. Wu and C. Leighton, Phys. Rev. B **67**, 174408 (2003).

[5] C. S. Snow, S. L. Cooper, D. P. Young, Z. Fisk, A. Comment, and J.-P. Ansermet, Phys. Rev. B **64**, 174412 (2001).

[6] S. A. Kivelson, E. Fradkin, and V. J. Emery, Nature (London) **393**, 550 (1998).

[7] T. Kimura, T. Goto, H. Shintani, K. Ishizaka, T. Arima, and Y. Tokura, Nature **426**, 55 (2003).

[8] A. P. Ramirez, J. Phys.: Condens. Matter **9**, 8171 (1997).

[9] A. N. Lavrov, S. Komiya, and Y. Ando, Nature **418**, 385 (2002).

[10] M. Kim, X. M. Chen, Y. I. Joe, E. Fradkin, P. Abbamonte, and S. L. Cooper, Phys. Rev. Lett. **104**, 136402 (2010).

[11] G. Lawes, A. P. Ramirez, C. M. Varma, and M. A. Subramanian, Phys. Rev. Lett. **91**, 257208 (2003).

[12] K. A. Gschneidner, Jr., V. K. Pecharsky, and A. O. Tsokol, Rep. Prog. Phys. **68**, 1479 (2005).

[13] R. Tackett, G. Lawes, B. C. Melot, M. Grossman, E. S. Toberer, and R. Seshadri, Phys. Rev. B **76**, 024409 (2007).

[14] C. Lacroix, P. Mendels, and F. Mila, *Introduction to Frustrated Magnetism: Materials, Experiments, Theory* (Springer, Berlin, 2011).

[15] R. W. McCallum, D. C. Johnston, C. A. Luengo, and M. B. Maple, J. Low Temp. Phys. **25**, 177 (1976).

[16] A. Irizawa, S. Suga, G. Isoyama, K. Shimai, K. Sato, K. Iizuka, T. Nanba, A. Higashiya, S. Niitaka, and H. Takagi, Phys. Rev. B **84**, 235116 (2011).

[17] M. Kopeć, J. R. Dygas, F. Krok, A. Mauger, F. Gendron, B. Jaszczak-Figiel, A. Gagor, K. Zaghib, and C. M. Julien, Chem. Mater. **21**, 2525 (2009).

[18] Y. Yamasaki, S. Miyasaka, Y. Kaneko, J.-P. He, T. Arima, and Y. Tokura, Phys. Rev. Lett. **96**, 207204 (2006).

[19] K. Dey, S. Majumdar, and S. Giri, Phys. Rev. B **90**, 184424 (2014).

[20] G. Giovannetti, A. Stroppa, S. Picozzi, D. Baldomir, V. Pardo, S. Blanco-Canosa, F. Rivadulla, S. Jodlauk, D. Niermann, J. Rohrkamp, T. Lorenz, S. Streltsov, D. I. Khomskii, and J. Hemberger, Phys. Rev. B **83**, 060402 (2011).

[21] A. Maignan, C. Martin, K. Singh, Ch. Simon, O. I. Lebedev, and S. Turner, J. Solid State Chem. **195**, 41 (2012).

[22] K. Singh, A. Maignan, C. Simon, and C. Martin, Appl. Phys. Lett. **99**, 172903 (2011).

[23] T. Suzuki and T. Katsufuji, Phys. Rev. B **77**, 220402 (2008).

[24] Y. Nii, H. Sagayama, H. Umetsu, N. Abe, K. Taniguchi, and T. Arima, Phys. Rev. B **87**, 195115 (2013).

[25] M. C. Kemei, J. K. Harada, R. Seshadri, and M. R. Suchomel, Phys. Rev. B **90**, 064418 (2014).

[26] H. J. Van Hook and M. L. Keith, Am. Mineral. **43**, 69 (1958).

[27] G. B. Jensen and O. V. Nielsen, J. Phys. C **7**, 409 (1974).

[28] B. Chardon and F. Vigneron, J. Magn. Magn. Mater. **58**, 128 (1986).

[29] J. H. Chung, K. H. Lee, Y. S. Song, T. Suzuki, and T. Katsufuji, J. Phys. Soc. Jpn. **82**, 034707 (2013).

[30] M. Kim, X. M. Chen, X. Wang, C. S. Nelson, R. Budakian, P. Abbamonte, and S. L. Cooper, Phys. Rev. B **84**, 174424 (2011).

[31] O. V. Nielsen, J. Cryst. Growth **5**, 398 (1969).

[32] N. Yamamoto, K. Nagasawa, Y. Bando, and T. Takada, Jpn. J. Appl. Phys. **11**, 1754 (1972).

[33] B. M. Wanklyn, J. Cryst. Growth **54**, 610 (1981).

[34] J. J. Couderc, S. Fritsch, M. Brieu, G. Vanderschaeve, M. Fagot, and A. Rousset, Philos. Mag. B **70**, 1077 (1994).

[35] M. Kim, Magnetic field- and pressure-tuned phases in $La_xPr_yCa_{1-x-y}MnO_3$ and Mn_3O_4: Inelastic light scattering studies and single crystal growth, Ph.D. thesis, University of Illinois at Urbana-Champaign 2011.

[36] A magnetic field sufficiently large to remove any signature of domains in a polarization study. In the present case, approximately 0.2 T.

[37] See,for example,Table I in K. Takubo, R. Kubota, T. Suzuki, T. Kanzaki, S. Miyahara, N. Furukawa, and T. Katsufuji, Phys. Rev. B **84**, 094406 (2011).

[38] S. L. Gleason, T. Byrum, Y. Gim, A. Thaler, P. Abbamonte, G. J. MacDougall, L. W. Martin, H. D. Zhou, and S. L. Cooper, Phys. Rev. B **89**, 134402 (2014).

[39] The peak at 54 cm^{-1} represents an excitation of the CDO phase with a relatively large cross-section, as seen in Fig. 5. A nonzero peak intensity at 54 cm^{-1} in the FCO phase is due to the presence of a small, remnant CDO phase fraction, as evidenced by a nonzero peak intensity at 295 cm^{-1}.

[40] The weak peak at 289 cm^{-1} indicates a minority FCO phase is present.

[41] See Fig. 3(a) in Ref. [10] and Fig. 8(a) in Ref. [30].

[42] F. Guillou, S. Thota, W. Prellier, J. Kumar, and V. Hardy, Phys. Rev. B **83**, 094423 (2011).